

## The enigmatic iron oxyhydroxysulfate nanomineral schwertmannite: Morphology, structure, and composition

REBECCA A. FRENCH,<sup>1,2,\*</sup> MANUEL A. CARABALLO,<sup>3</sup> BOJEONG KIM,<sup>1,2</sup> J.D. RIMSTIDT,<sup>2</sup>  
MITSUHIRO MURAYAMA,<sup>4,5</sup> AND MICHAEL F. HOHELLA JR.<sup>1,2</sup>

<sup>1</sup>ICTAS Environmental Nanoscience and Technology Laboratory, Virginia Tech, Blacksburg, Virginia 24061, U.S.A.

<sup>2</sup>Department of Geosciences, Virginia Tech, Blacksburg, Virginia 24061, U.S.A.

<sup>3</sup>Geology Department, University of Huelva, Campus “El Carmen”, E-21071 Huelva, Spain

<sup>4</sup>ICTAS Nanoscale Characterization and Fabrication Laboratory, Virginia Tech, Blacksburg, Virginia 24061, U.S.A.

<sup>5</sup>Department of Materials Science and Engineering, Virginia Tech, Blacksburg, Virginia 24061, U.S.A.

### ABSTRACT

Two sets of precipitates collected from stream sediments in the Monte Romero (MR) and Tinto Santa Rosa (TSR) abandoned mine sites—located in the Iberian Pyrite Belt (IPB) of Spain—were identified as the iron oxyhydroxysulfate nanomineral schwertmannite using X-ray diffraction (XRD) and bulk digestion and were further studied in great detail using analytical high-resolution transmission electron microscopy (HRTEM). Extensive HRTEM observations suggest that schwertmannite should not be described as a single-phase mineral with a repeating unit cell, but as a polyphasic nanomineral with crystalline areas spanning less than a few nanometers within an amorphous matrix. The *d*-spacings measured from lattice fringes within schwertmannite’s needles match with *d*-spacings of the known transformation products of schwertmannite (goethite and jarosite). This finding implies that the initial stages of schwertmannite transformation occur as a gradual structural reordering at the nanoscale. Energy-dispersive X-ray analysis applied across individual schwertmannite needles with ~3 nm spot size resolution reveal a decreasing ratio of sulfur to iron and silicon to iron from the surface of the needle to the core with the silicon to iron ratio consistently higher than the sulfur to iron ratio. Amorphous silicon-rich precipitates were identified on the surface of the TSR schwertmannite. All of these observations explain why the measured solubility product of schwertmannite is variable, resulting in calculated stability fields that differ greatly from sample to sample. Arsenic is the most abundant trace element in these samples [MR: 0.218(1) wt% and TSR: 0.53(2) wt%], keeping in mind that schwertmannite has been shown to be a key player in the cycling of this element on a global basis, particularly from the IPB. Furthermore, arsenic in the TSR schwertmannite is associated with crystalline areas within its needle matrix, implying that schwertmannite-derived goethite nanocrystals may be an important host of arsenic.

**Keywords:** Nanomineral, schwertmannite, goethite, jarosite, iron oxide, arsenic, silicon, sulfate

### INTRODUCTION

The ferric oxyhydroxysulfate nanomineral schwertmannite [Fe<sub>8</sub>O<sub>8</sub>(OH)<sub>8-x</sub>(SO<sub>4</sub>)<sub>x</sub> (1 < x < 1.75)] was officially recognized as a mineral in 1994 (Bigham et al. 1994). The proposed structure for schwertmannite was a modified akaganéite structure where sulfate occupies the tunnels formed by FeO<sub>6</sub> octahedra in a bridged bidentate complex, in place of chloride anions as in akaganéite. Fernandez-Martinez et al. (2010) recently refined the positions of iron and O atoms in the Bigham et al. (1994) proposed structure using pair distribution function (PDF) analysis of high-energy X-ray total scattering experiments and concluded that schwertmannite consists of a “highly defective entangled network of structure motifs.” The defects in the iron octahedral framework would result in a strained structure. Modeling of the synchrotron powder X-ray diffraction

(XRD) patterns revealed that the best model structure would contain two inner-sphere and two outer-sphere sulfate anions per unit cell. PDF analysis has advanced the understanding of the structure of poorly crystalline nanominerals relative to conventional XRD analysis as for example in Michel et al.’s (2007, 2010) refinement of the ferrihydrite structure, but this work has also been criticized. Manceau (2009, 2010, 2011) argued that the proposed structure violates Pauling’s second and third principles. Moreover, Manceau (2011) warned that PDF does not provide sufficient information to obtain unique crystallographic structures of defective minerals and in particular for nanocrystalline materials.

As suggested by the model structure in Fernandez-Martinez et al. (2010), analysis of the schwertmannite structure must also take into account the existence of multiple phases and defective structures. The widely ranging bulk chemistry presented by schwertmannite and the significant variations in the conditions of its formation imply the existence of a broad range of

\* E-mail: rafrench@vt.edu

calculated solubility constants (Bigham et al. 1996b; Kawano and Tomita 2001; Yu et al. 1999) that result in a pH stability window ranging from pH ~2–3 to pH ~2–7.5, depending on the solubility product used (Majzlan et al. 2004a). The predictive ability of geochemical models for schwertmannite's stability is further hindered by the fact that its predicted stability field may overlap with that of ferrihydrite and jarosite, both of which also have a range of calculated solubilities (Bigham et al. 1996b). Bigham et al.'s field samples also reflect these overlapping stability fields as many samples are mixtures of schwertmannite, ferrihydrite, jarosite, and/or goethite. Generally, though, they found that schwertmannite dominated precipitates collected in waters with a pH of 2.8 to 4.5 and ferrihydrite dominated in waters above pH 6.5. Furthermore, schwertmannite is metastable with respect to goethite and jarosite under conditions where goethite and jarosite typically form (Acero et al. 2006; Asta et al. 2010a), but the rate of transformation may vary anywhere from hours (Burton et al. 2008) to years (Bigham et al. 1996b; Jonsson et al. 2005; Regenspurg et al. 2004) depending on geochemical conditions. Despite its unpredictability, researchers continue to incorporate schwertmannite into geochemical models because schwertmannite has been widely found as a precipitate in acid mine drainage (AMD) systems (Bigham et al. 1994, 1996b; Espana et al. 2005), mine pit lakes (Blodau 2006; Peine et al. 2000; Regenspurg et al. 2004), and acid-sulfate soils (Burton et al. 2006, 2007). It has also been found in acid oxic microenvironments in glacial and iceberg sediments (Raiswell et al. 2009). Schwertmannite preserved in icebergs may then become a source of bioavailable iron in oceans (Raiswell 2011). Finally, the same processes that produce schwertmannite in AMD systems may also have occurred on the surface of Mars (Caraballo et al. 2011; Fernandez-Remolar et al. 2004), making schwertmannite a mineral of interplanetary importance.

High-resolution transmission electron microscopy (HR-TEM) allows researchers to discern polyphasic crystal morphology and atomic structure at the nanoscale. Using this technique, researchers have shown the existence of non-classical crystal growth mechanisms, such as oriented-attachment of crystalline nanoparticles in material that would have appeared poorly crystalline or amorphous using XRD analysis (Banfield et al. 2000; Moreau et al. 2004). HRTEM has also been used to evaluate crystal face dependent dissolution of mineral nanoparticles (Liu et al. 2008, 2009). Researchers used analytical-HRTEM to identify mineral nanoparticles carrying toxic trace metals in a river system over long distances that would have otherwise not been predicted (Plathe et al. 2010). It has also proved to be a useful tool in the discovery of new nanophases of minerals (Hochella et al. 1999) and in the fate and transformation of engineered nanomaterials in waste streams (Kim et al. 2010). Despite the promise that HRTEM shows for giving new insights into schwertmannite's morphology, structure, and composition, no studies have applied HRTEM to natural samples of schwertmannite at the resolution needed to investigate it at the nano- and atomic scale.

In this study, we present the first HRTEM study of natural schwertmannite, these specimens collected from abandoned mine sites in the Iberian Pyrite Belt (IPB) of southwest Spain. The IPB is a world-class site in which to study schwertmannite.

The IPB is one of the largest sulfide provinces in the world, spanning across the Huelva Province of Spain and continuing into Portugal with an estimated 1700 Mt of original sulfide ore reserves, the main mineral of which is pyrite (Saez et al. 1999). Thousands of years of mining these deposits for valuable trace metals left hundreds of abandoned mines and significant pollution in the form of largely unchecked acid mine drainage (AMD) (Sarmiento et al. 2007). The AMD drains to the Odiel River basin and the Tinto River and subsequently to the Gulf of Cádiz and the Atlantic Ocean. Olias et al. (2006) estimated that the Odiel and Tinto rivers transport 7922 tons/year of iron and 183 802 tons/year of sulfate, which represents 0.32% and 0.15% of the total global riverine flux of these chemical components. Furthermore, they estimated that these rivers transport 0.15%, 3.13%, and 15.1% of the global riverine flux of arsenic, copper, and zinc, respectively. A survey of 64 AMD discharges from 25 different mines in the IPB (Espana et al. 2005) determined that schwertmannite was the "most important mineral phase, both in controlling the Fe solubility at pH 2–4, and as a sorbent of the trace elements (As, Cu, Zn)," effectively assigning schwertmannite a significant part of the global cycling of these elements, remarkably, from this single region.

## MATERIALS AND METHODS

### Field site and sampling description

Schwertmannite and water samples were collected from two abandoned mines in the Iberian Pyrite Belt (IPB) of southwest Spain. The Monte Romero (MR) mine contains a massive pyrite deposit rich in zinc, lead, and copper sulfides. The enclosing rocks are siliciclastic schists without carbonate beds (Pinedo-Vara 1963). The main ore of the Tinto Santa Rosa (TSR) mine mainly consists of pyrite, chalcopyrite, and arsenopyrite. After the closure of the mine and recovery of groundwater levels, water began to flow from one of the mine adits and formed the TSR stream. In both mine sites, fresh precipitates were collected from the stream bed sediment. In the MR site, the iron precipitates appear as fine and loose orange sediment (Fig. 1a). Iron precipitates in the TSR site have formed iron terraces of iron-rich stromatolites (Perez-Lopez et al. 2011) in the stream bed and samples were collected from the surface of these terraces (Fig. 1b). To avoid the presence of aged iron mineral phases in the deeper sediments, only the top 1–2 cm of the fresh precipitates were collected. The samples were air dried at room temperature in the laboratory to avoid any mineral phase transformation and were ground to a powder using an agate mill.

Water samples were collected near the solid samples. Methods were based on previous field studies on acid mine drainage sites within the IPB (Caraballo et al. 2009, 2011). After filtering the water through a 0.1  $\mu\text{m}$  Millipore filter on Millipore syringe filter holders, the samples were acidified in the field to pH 1 with concentrated nitric acid and stored at 4 °C in polyethylene bottles until analysis. Temperature and electrical conductivity were measured in the field using a portable CM35 meter (Crison) with 3 point calibration (147 and 1413  $\mu\text{S cm}^{-1}$  and 12.88  $\text{mS cm}^{-1}$ ). The pH and redox potential (Eh) were measured using a PH25 meter (Crison) with Crison electrodes. Eh and pH were controlled and calibrated using 2 points (240–470 mV) and 3 points (pH 4.01–7.00–9.21), respectively, with Crison standard solutions. An auto-calibrating Hanna portable meter was used to measure dissolved  $\text{O}_2$ .

### River and sediment sample analysis

Concentrations of dissolved Al, As, Ca, Cd, Co, Cr, Cu, Fe, K, Mg, Mn, Ni, Pb, S, Si, Ti, V, and Zn in the river samples were determined by inductively coupled plasma-atomic emission spectrometry (ICP-AES Jobin-Yvon Ultima2) using a protocol especially designed for AMD samples (Tyler et al. 2004). Analysis was performed at the Central Research Services at the University of Huelva (CRSUH). Multi-element standard solutions (SCP SCIENCE) were run at the beginning and end of each analytical series for calibration. Certified Reference Material SRM-1640 NIST freshwater-type and inter-laboratory standard IRMM-N3 wastewater test materials (European Commission Institute for Reference Materials and Measure-



FIGURE 1. Schwertmannite precipitates from the Monte Romero mine site (a) and the Tinto Santa Rosa creek with iron terraces (b). (Color online.)

ments) were also analyzed. No significant differences were found between the certified values and the measured concentrations. Samples were run in triplicate and the relative standard deviation of the measured concentrations was less than 5%. Detection limits were calculated by average and standard deviations from 10 blanks. Detection limits were: 0.200 mg/L for Al, Fe, Mn, Mg, Si, and S; 0.5 mg/L for Ca; 0.05 mg/L for Zn; 0.005 mg/L for Cu; 0.002 mg/L for As; and 0.001 mg/L for the other trace elements.

The iron precipitates were first digested using concentrated nitric acid. About 0.05 g of iron precipitates were mixed with 3 mL of concentrated nitric acid (ACS grade) and were left sitting closed at room temperature in digest vessels (CEM MARSXpress acid digest vessel) for three or more days until colored solids were no longer visible. The samples were then diluted with NANOpure water (Barnstead, 18.2M $\Omega$ -cm water with 1–5 ppb TOC) to a total volume of 25 mL. The samples were analyzed using ICP-AES (Spectro ARCOS ICP Model FHS16, Virginia Tech Soil Testing Laboratory) for the concentrations of Al, As, Ca, Cd, Co, Cr, Cu, Fe, K, Mg, Mn, Ni, Pb, S, Si, Ti, V, and Zn. Calibration standards were prepared for each single element within the matrix solution of 12% nitric acid. A blank with 12% nitric acid was run as well and all analyzed metals were below detection limits. Quality control (QC) standards with a “Certificate of Analysis” were prepared from multielement standards that are used for verification of instrument accuracy and precision throughout the analysis. A QC check of 90–110% of the true value is considered acceptable. White solids, most likely silicates that would not be dissolved by a nitric acid digestion, were visible in the MR samples. These solids were filtered out of solution using a 0.1  $\mu$ m syringe filter (Acrodisc, Supor membrane) before ICP-AES analysis. Three replicates were analyzed for each sample and the concentration was reported as the average and twice the standard deviation or the 95% confidence interval. Detection limits were Al 6, As 17, Ca 51, Cd 4, Co 7, Cr 7, Cu 7, Fe 7, K 41, Mg 36, Mn 3, Na 16, Ni 6, Pb 16, S 51, Si 65, Ti 11, and Zn 6  $\mu$ g/L. This digestion method will not completely dissolve silicate minerals and therefore the total metal analysis in this study would not reflect the total amount of the elements in the samples (e.g., Si, Al, Fe, K, Mg, Ca, etc.).

### Geochemical modeling

The equilibrium geochemical speciation/mass transfer model PHREEQC (Parkhurst 1995) with the database of the speciation model MINTEQA2 (Ball and Nordstrom 1991) was used to calculate the saturation indices (SI) ( $SI = \log IAP - \log K$ , IAP = ion activity product) of possible iron oxide phases in the field sites and the aqueous speciation of metals in the water samples. Additional thermodynamic data for schwertmannite were taken from Yu et al. (1999) and Kawano and Tomita (2001). Zero, negative, or positive SI values predict whether the field sites were in equilibrium, undersaturated, or supersaturated, respectively, with goethite, ferrihydrite, jarosite, and schwertmannite.

### Powder X-ray diffraction

The purity of the schwertmannite samples was determined using powder X-ray diffraction on a PANalytical X-pert PRO diffractometer with a  $CuK\alpha$  (45 kV to 40 mA) radiation. Analysis was performed from 10.004 to 79.976  $^{\circ}2\theta$  with a step size of 0.017 $^{\circ}$ .

### Transmission electron microscopy (TEM) sample preparation and mounting

TEM ultramicrotomed thin sections of schwertmannite were prepared to examine bulk morphology (e.g., needle length and schwertmannite core morphology), but not for atomic structure analysis because the following preparation method could affect the schwertmannite structure. The thin sections were prepared using a method with Poly/Bed 812 (Polysciences, Inc., Data Sheet 233). Subsamples of the selected schwertmannite were mixed with NANOpure water in a 2 mL centrifuge tube and then dehydrated by applying a series of ethanol solutions from graded 15 to 100% ethanol to water. After completing dehydration, the precipitates were placed in 100% propylene oxide for 15 min, followed by infiltration with a suspension of propylene oxide and Poly/Bed 812 [50:50 (v:v)] and left overnight. On the following day, the samples were again subjected to infiltrate with 100% of Poly/Bed 812 and left to sit overnight. The following day, the samples were embedded in a flat mold using freshly prepared 100% Poly/Bed 812. The mold was then cured in an oven set at 60  $^{\circ}C$  for at least 48 h. Ultra-thin sections were obtained by ultramicrotome using a diamond knife and approximately 60–90 nm thick sections were collected on a copper or gold TEM grid with a lacey carbon support film.

Whole schwertmannite aggregates that were examined by HRTEM as a structural analysis tool were prepared from samples that had been air dried and stored at room temperature with no further treatment. The aggregates were dispersed on TEM grids using the following two methods: (1) iron precipitates were suspended in NANOpure water and placed in a sonicating bath for 5 min to disperse aggregates and (2) iron precipitates were suspended in ethanol and placed in a sonicating bath for 2 min to disperse aggregates. In both sample preparations, a droplet of sample was placed on a copper or gold TEM grid with a lacey carbon support film and wicked dry with a Kimwipe. TEM grids were then placed in a desiccator under vacuum until analysis. There were no differences observed in TEM images collected on schwertmannite prepared using these two sample preparation methods.

These samples were found to be stable under the beam conditions used for the duration of the time needed to collect HRTEM images. No change in the schwertmannite needle morphology was observed at any time. The structures observed in this study were consistent across images of schwertmannite collected during different instrument sessions, on different instruments, and on different schwertmannite particles, indicating that the structures observed were not simply an artifact of interaction with an electron beam. Furthermore, although this is the first HRTEM study on natural schwertmannite, the crystalline nanostructures observed here are consistent with previously published work on the structure of synthetic schwertmannite using HRTEM (Hockridge et al. 2009). In that study, care was also taken to ensure that the schwertmannite samples were not damaged by the beam.

### Microscopy and chemical analysis

Whole schwertmannite aggregates on TEM grids, as prepared above, were scanned for arsenic using an environmental scanning electron microscope (ESEM) (FEI Quanta 600 FEG) with energy-dispersive X-ray spectroscopy (EDX) (Bruker

QUANTAX 400) operating at 20 kV. This technique allowed us to locate samples with a sufficiently high arsenic concentration that would be detectable on the EDX on TEM. Seventy-four aggregates of schwertmannite from the TSR mine site, displaying the characteristic “pin-cushion” morphology and strong iron and sulfur signals, were scanned. Approximately 70% of those aggregates showed an L peak for arsenic indicating that arsenic was present at detectable levels in those aggregates. Silicon was not detectable above background levels using ESEM/EDX. Images of the grid location of each schwertmannite aggregate were collected to locate the same aggregate during TEM analysis.

TEM imaging and EDX analysis were performed on an FEI Titan 300 operating at 200 kV (ICTAS NCFL, Virginia Tech), FEI Titan 300 TEM operating at 300 kV (Department of Materials Science and Engineering, University of Virginia), and an FEI Titan3 operating at 300 kV (FEI demo lab, CEOF Ohio State University). TEM images were analyzed using fast Fourier transform (FFT) in the Digital Micrograph software program with supplemental software [SADP Tools (Wu et al. 2012)] to measure *d*-spacings from FFT images. Where possible, lattice fringes were directly measured by hand using ImageJ (Abramoff et al. 2004), corroborating *d*-spacings determined from FFT analysis. When lattice fringes were measured using ImageJ, the error was determined by the standard deviation of at least three measurements. The *d*-spacing error using FFT analysis depends upon the pixel size of the images.

Analysis of EDX peaks was performed with a background correction that uses a multi-polynomial fit of background bremsstrahlung radiation, which is caused by deceleration of incident electrons. The characteristic peaks were fitted with a Gaussian curve and peak intensity was recorded. The default setting on the software recognizes peaks as significant only if they are six times higher than the background intensity. Ratios of silicon to iron, sulfur to iron and arsenic to iron were calculated based on the integrated intensity of the K peaks for the respective elements. Silicon and sulfur have adjacent peaks in EDX spectra and have *k*-factors that are very close to one. The ratios of sulfur to iron and silicon to iron may therefore be directly compared as relative concentrations of the elements. Absolute concentrations of elements were not measurable due to unknown sample thickness.

The chemical composition of individual needles on the surface of schwertmannite particles were analyzed by focusing the beam to a ~3 nm spot and collecting EDX data at that point. The beam was then manually moved to an adjacent area and data was again collected. The schwertmannite sample was significantly damaged during these analyses in the immediate vicinity of the beam (Supplementary Fig. 1'), but the small amounts of material in the needles at this lateral resolution necessitated this approach to obtain sufficient signal for analysis. TEM images were collected on the undamaged schwertmannite areas before EDX data collection to correlate needle morphology and structure with chemical information.

Electron tomography was performed with the FEI Titan 80-300 TEM operated at 200 kV. Tilt-series were acquired in high-angle annular dark field (HAADF)—scanning transmission electron microscope (STEM) mode using a Fischione Model 3000 annular dark-field detector at a beam convergence (half-angle) of 10.5 mrad and a Fischione 2020 ultra-high tilt single-axis tomography holder. Images were recorded every 2° in the tilt range of -65 to +65°. Hardware calibrations and software parameters were refined to improve tilt series acquisitions at high magnification. These parameters included: defocus, image shift, and specimen holder tilt shift. Following an acquisition of a tilt series, images were spatially aligned by cross-correlation algorithm using FEI Inspect 3D Express software. A simultaneous iterative reconstruction technique (SIRT) was used to reconstruct data sets and 3D visualization was performed using FEI Resolve RT.

<sup>1</sup> Deposit item AM-12-060, 13 supplemental figures and a video file. Deposit items are available two ways: For a paper copy contact the Business Office of the Mineralogical Society of America (see inside front cover of recent issue) for price information. For an electronic copy visit the MSA web site at <http://www.minsocam.org>, go to the *American Mineralogist* Contents, find the table of contents for the specific volume/issue wanted, and then click on the deposit link there.

## RESULTS AND DISCUSSION

### Field site and bulk schwertmannite mineralogy and chemical analysis

The water chemistry and metal content of the stream water in MR and TSR sites (Table 1) create conditions that favor schwertmannite formation in the IPB, with a low pH between 2 and 4, oxic conditions and high dissolved sulfate and iron (España et al. 2005). Saturation indices calculated using PHREEQC for the mines sites (Table 2) shows that using the Bigham et al. (1996b) solubility constant, the sites are undersaturated with respect to schwertmannite, whereas the solubility constants reported by Yu et al. (1999) and Kawano and Tomita (2001) predict that these sites are near saturation or supersaturated with respect to schwertmannite. Calculations also predict that both sites are supersaturated with respect to goethite and that the MR site is supersaturated with respect to K-jarosite and H<sub>3</sub>O-jarosite. Previous studies on the MR site and TSR site also found that the solubility constants calculated by Yu et al. (1999) more accurately reflected the mineralogy of the field site and H<sub>3</sub>O-jarosite was the identified jarosite phase (Acero et al. 2006; Asta et al. 2010b).

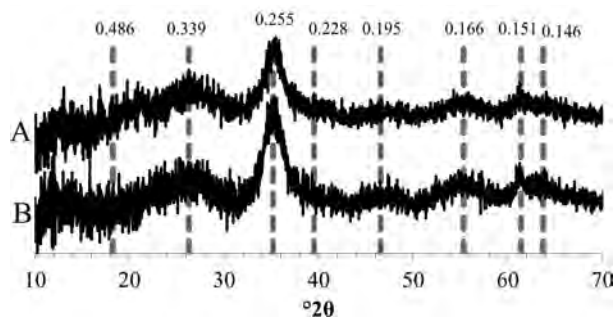


FIGURE 2. XRD pattern for precipitates from the two sampling sites, the Monte Romero mine (A) and the Tinto Santa Rosa mine (B). The gray dotted lines are the reported *d*-spacings for schwertmannite (Cornell and Schwertmann 2003).

TABLE 1. Water chemistry of AMD streams (element concentration = mg/L)

Site	pH	CE (mS/cm)	T (°C)	Eh (mV)	pE
MR	2.66	2.76	30	672.2	11.4
TSR	2.53	2.53	18.4	660	11.2

Site	Al	As	Ca	Cd	Co	Cr	Cu	Fe	K	Mg
MR	105	0.085	260	0.701	0.775	0.0043	5.9	201	3.1	264
TSR	66	0.791	162	0.079	0.954	0.011	15	568	n.d.*	124

Site	Mn	Ni	Pb	S	Si	Ti	V	Zn
MR	18	0.826	0.139	1136	38	0.007	n.d.	457
TSR	33	0.731	0.076	902	33	n.d.	0.00973	62

Notes: n.d. = no data. R.S.D. of element concentrations = <5%.

TABLE 2. Saturation index (SI) calculated with PHREEQC Interactive 2.15.0 for goethite, ferrihydrite, jarosite, and schwertmannite

Site	Goethite	Fe(OH) <sub>3</sub>	K-jarosite	H <sub>3</sub> O-jarosite	Schwertmannite [logK = 18(2.5)]*	Schwertmannite [logK = 10.5(2.0)]†	Schwertmannite [logK = 7.06(0.09)]‡
MR	4.3	-1.8	2.4	0.39	-5.2	0.84	10.0
TSR	3.7	-2.0	n.d.	-1.2	-6.1	-0.027	8.90

Note: Three different solubility constants were employed to calculate schwertmannite's SI.

\*  $\text{Fe}_8\text{O}_8(\text{OH})_{4.5}(\text{SO}_4)_{1.6} + 20.8\text{H}^+ = 8\text{Fe}^{3+} + 1.65\text{SO}_4^{2-} + 12.8\text{H}_2\text{O}$  (Bigham et al. 1996a).

†  $\text{Fe}_8\text{O}_8(\text{OH})_{4.4}(\text{SO}_4)_{1.8} + 20.4\text{H}^+ = 8\text{Fe}^{3+} + 1.8\text{SO}_4^{2-} + 12.4\text{H}_2\text{O}$  (Yu et al. 1999).

‡  $\text{Fe}_8\text{O}_8(\text{OH})_{5.5}(\text{SO}_4)_{1.05} + 21.9\text{H}^+ = 8\text{Fe}^{3+} + 1.05\text{SO}_4^{2-} + 13.9\text{H}_2\text{O}$  (Kawano and Tomita 2001).

Schwertmannite collected at the TSR and MR sites exhibits the characteristic X-ray diffraction pattern for schwertmannite with broad peaks, although the peak at 0.486 nm was too weak to distinguish in our XRD analysis (Fig. 2). However, Perez-Lopez et al. (in preparation) identified all eight peaks of these same schwertmannite samples using synchrotron micro-XRD. The two XRD patterns in Figure 2 are nearly identical with the center of the peaks aligning, but the MR pattern exhibits lower

peak intensity, most visible in the peak at 0.255 nm.

Bulk digestion of the schwertmannite samples showed that the most abundant elements were iron and sulfur with approximately the same average weight percent of each element for both samples (Table 3). If we use the model structure for schwertmannite (Bigham et al. 1994; Yu et al. 1999) and hold the number of atoms of iron and oxygen as a constant of 16 atoms, then we can calculate the formula for schwertmannite for the MR

**TABLE 3.** Elemental composition of schwertmannite samples (wt%)

Site	Al	As	Ca	Cd	Co	Cr	Cu	Fe	K	Mg
MR	0.125(4)*	0.218(1)	0.072(8)	b.d.l.†	b.d.l.	b.d.l.	0.0148(4)	41.9(5)	0.007(4)	0.07(2)
TSR	0.023(5)	0.53(2)	0.010(1)	b.d.l.	b.d.l.	b.d.l.	0.0053(3)	42.0(7)	b.d.l.	b.d.l.
Site	Mn	Ni	Pb	S	Si	Ti	V	Zn		
MR	0.0015(9)	b.d.l.	b.d.l.	5.5(3)	0.008(3)	0.0040(7)	0.0215(3)	0.011(3)		
TSR	0.0009(9)	b.d.l.	b.d.l.	5.5(4)	0.05(1)	b.d.l.	0.010(3)	0.0026(8)		

\* Numbers in parentheses = e.s.d. or twice the standard deviation (95% confidence).

† b.d.l. = below detection limit.

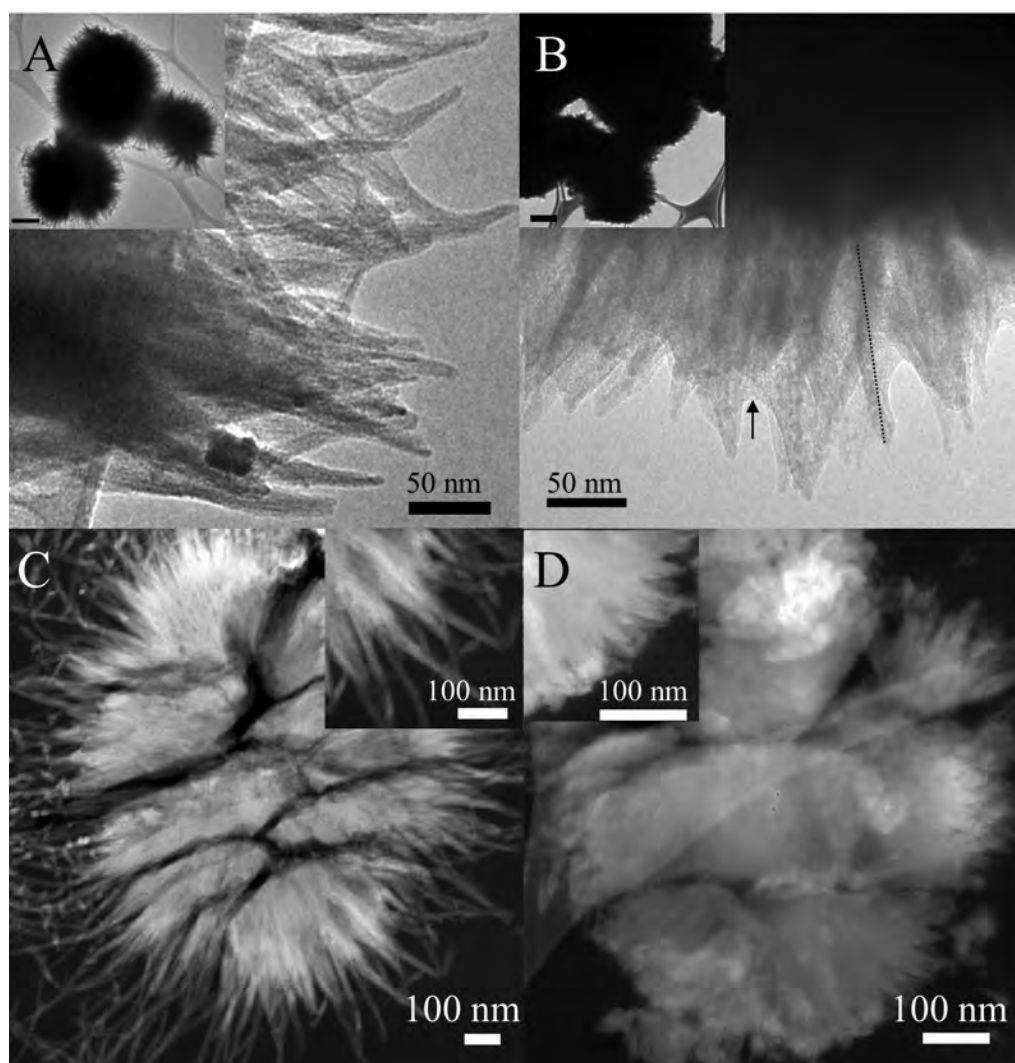


**FIGURE 3.** Schwertmannite needles from a schwertmannite “pin cushion” shown in inset (inset scale bar = 500 nm) from the Monte Romero mine (a) and the Tinto Santa Rosa mine (b) sites and a cross section of a schwertmannite particle embedded in resin from the Monte Romero mine (c) and the Tinto Santa Rosa mine (d) taken in HAADF-STEM mode. Insets show magnifications of needles on the surface of the schwertmannite particle.

as  $\text{Fe}_{16}\text{O}_{16}(\text{OH})_{8.68}(\text{SO}_4)_{3.66}$  and for the TSR schwertmannite as  $\text{Fe}_{16}\text{O}_{16}(\text{OH})_{8.72}(\text{SO}_4)_{3.64}$ . The number of sulfates in this formula is in good agreement with the model proposed by Fernandez-Martinez et al. (2010) with two outer-sphere and two inner-sphere complexes of sulfate per unit cell.

After iron and sulfur, arsenic was the most abundant element measured in both samples and is an order of magnitude higher in concentration than any other measured element in the precipitates with the exception of aluminum in the MR schwertmannite and calcium in the TSR schwertmannite. Previous field studies on the MR and TSR sites also showed that schwertmannite was a major sink for arsenic (Acero et al. 2006; Asta et al. 2010b).

### Characterization of schwertmannite morphology and needle structure

Needles on the surface of the MR schwertmannite measure approximately 150–250 nm in length and 5–20 nm in width (Fig. 3a), which falls within the range of reported needle length from previous studies (Bigam and Nordstrom 2000). It is difficult though to define where a particular needle begins as the needles are densely packed. In the core the bundles of needles are too electron dense to differentiate between them. Many needles appear to consist of two or more separate needles at the base, but then grow together to form a single tip. The needles are also tapered and become thinner from the center of the schwertmannite particle to the surface. They do not exhibit any faceting and appear rounded at the tips.

The TSR schwertmannite has shorter and wider needles than the MR schwertmannite (Fig. 3b). The needle length, measured from the intersection of two needles to the tip (see arrow Fig. 3b for example) is <50 nm. However, if the length is measured from a more electron dense area to the edge of the darkest part of the TEM image, then the needles measure approximately 100–150 nm in length (see dotted line Fig. 3b for example). The width of the needles, 5–20 nm is approximately the same for both the MR and TSR schwertmannite samples.

In cross-section view, the longer needles on the MR schw-

ertmannite particle are 250–300 nm long (Fig. 3c), whereas needles on the TSR schwertmannite particle are 30–50 nm long (Fig. 3d). Other TSR schwertmannite images (Supplemental Fig. 2<sup>1</sup>) also showed schwertmannite with longer needles on the same length scale as the MR schwertmannite, indicating heterogeneous needle length across schwertmannite particles.

To date no one has been able to determine whether or not schwertmannite has a solid core or is made up of densely packed needles (Loan et al. 2004). In the MR schwertmannite (Fig. 3c), features that resemble densely packed needles (e.g., porous areas shown by a darker contrast) extend ~200 nm from the base of the needles into the core. Assuming a spherical particle and that this schwertmannite particle was cut at the center of the sphere, the needles would make up greater than 70% of the volume of the schwertmannite particle. In the TSR schwertmannite, the needles extend ~50 nm into the core, yielding a needle volume of 36% of the entire schwertmannite particle. This estimate does not intend to imply that needles do not make up the entire core of the schwertmannite particle, but to demonstrate that a high proportion of the volume of schwertmannite aggregates are made up of needles. A movie (Supplemental material<sup>1</sup>) prepared using tomography shows high-electron density within the core of the three dimensional representation of the schwertmannite particles, but again the needles appear to dominate the schwertmannite morphology. Investigating the structure of the entire core of schwertmannite remains a continuing challenge. Unfortunately obtaining a sufficiently thin sample and artifacts from beam interaction with the resin prevented the examination of structural motifs (e.g., lattice fringes, etc.) on these samples using HRTEM.

The uniform contrast seen in the needles of the MR schwertmannite at lower magnifications (Fig. 3a) is also observed at higher magnifications with atomic resolution. A single needle from the area shown in Figure 3a is pictured in Figure 4. The edges and tip of the needle do not display any distinct facets and have an atomically rough surface. There are no lattice fringes that extend throughout the needle, but instead, in the places

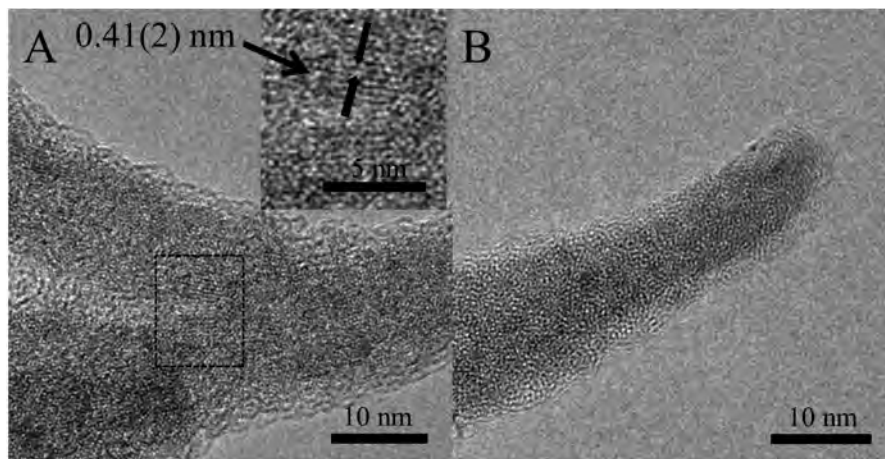


**FIGURE 4.** TEM images of an individual schwertmannite needle from the Monte Romero mine on the surface of one of the schwertmannite particles in Figure 2a. The base of the needle is shown in **a** and the tip of the same needle is shown in **b**. Inset in **a** shows magnified area of the lattice fringes enclosed by the black box. The  $d$ -spacing [0.41(2) nm] does not match the schwertmannite XRD pattern, but it does match the (101) peak in the goethite XRD pattern (see Supplemental Figure 3<sup>1</sup>). See text for details.

where they can be recognized at all, the fringes are continuous for no more than 4 nm, and in places are apparent for only 1 nm. This suggests an assemblage of very small nanocrystals, but the edges of individual particles are not visible within the needle. One area in the needle displays measurable lattice fringes that do not correlate with any schwertmannite peak in the XRD pattern, but the  $d$ -spacing does match the spacing for the (101) plane of goethite at 0.41 nm (Supplemental Fig. 3<sup>1</sup>).

A thicker schwertmannite needle (Fig. 5, left) from another schwertmannite particle from the MR site (Supplemental Fig. 8<sup>1</sup>) illustrates the highly disordered nature of the schwertmannite. No individual spots are discernable within the fast Fourier transformation (FFT) pattern, only a broad ring (Fig. 5, left inset). The width of the ring gives a range of  $d$ -spacings that overlap with the most intense peak of the schwertmannite XRD pattern. FFT analysis on another needle from the same MR schwertmannite particle (Fig. 5, right) displays a single pair of bright spots within the otherwise noisy pattern. The  $d$ -spacing measured from these spots also aligns with the intense 0.255 nm peak for schwertmannite. The water chemistry data (Table

2) indicates that this site is supersaturated with respect to goethite and jarosite, both of which have planes with  $d$ -spacings that could match the  $d$ -spacing of the FFT spots as well (Table 4). Details on the FFT error analysis and graphs including the  $d$ -spacing and error for Tables 4–6 are provided in the supplemental information<sup>1</sup>. Noisy areas in the FFT pattern could be due to a poorly ordered structure, crystals that are not oriented correctly with respect to the incident electron beam to diffract, and/or overlapping crystals (Janney et al. 2000).

The TSR schwertmannite displays differences in crystallinity between a needle (seen by the darker contrast) and the space between the two needles (no visible fringes and lighter contrast) (Figs. 6 and 3b). FFT analysis of crystalline areas reveals that most of the  $d$ -spacings measured from lattice fringes aligns with the 0.255 and 0.228 nm XRD peaks for schwertmannite and goethite reflections in those areas (Tables 5 and 6). One lattice fringe, and its respective  $d$ -spacing aligns with the XRD peak located at 0.339 nm, had no matching goethite plane. However, the second and third most intense peaks in H<sub>3</sub>O-jarosite's XRD pattern could match this  $d$ -spacing (Table 5). Geochemical

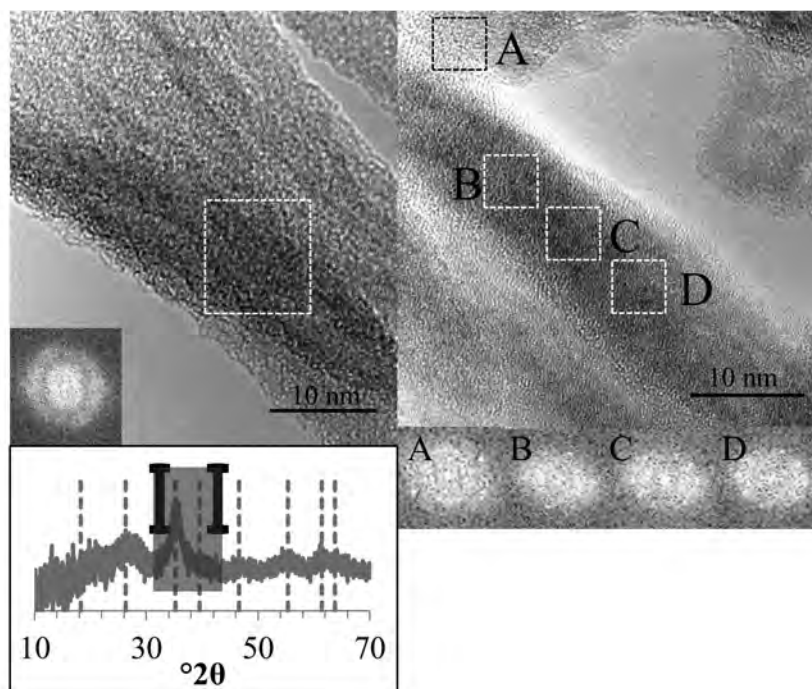


**FIGURE 5.** TEM images of needles on the surface of a schwertmannite particle from the Monte Romero mine. Insets show the FFT patterns of the areas enclosed by the white dashed boxes. The XRD pattern is the same schwertmannite pattern shown in Figure 2a, with the gray dotted lines marking the positions of schwertmannite  $d$ -spacings (Cornell and Schwertmann 2003). The black lines on the XRD pattern give the location of the  $d$ -spacings measured from the inside and outside edge of the outer diffuse ring on the FFT pattern (inset, left TEM image). See text for details. See Supplemental Figure 4<sup>1</sup> for explanation of how error bars are calculated.

**TABLE 4.** The  $d$ -spacings measured from FFT analysis of lattice fringes (Fig. 5, right image) and the corresponding peak in the schwertmannite, goethite, and H<sub>3</sub>O-jarosite XRD patterns\*

Image area	Schwertmannite XRD peak (nm)	Goethite planes	H <sub>3</sub> O-jarosite planes†
A,B	0.255/0.228	A,B: (211) (002) (111); A: (011)	A,B: (107) (205); A: (024)
C,D	0.255	C,D: (111) (400) (011) (210)	C,D: (205) (024)

\* See Supplemental Figure 4<sup>1</sup> for exact locations of  $d$ -spacings, including error bars.

† Majzlan et al. (2004b).

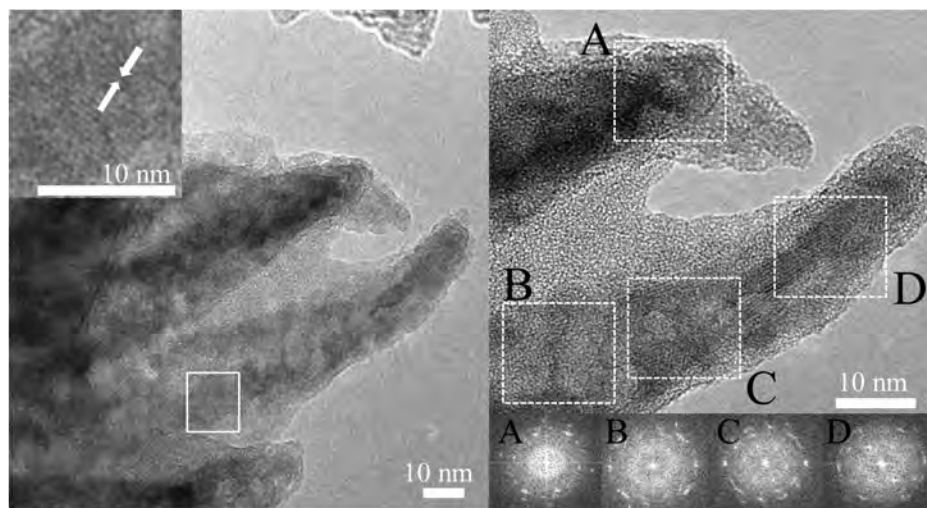


**FIGURE 6.** Needles on the surface of a schwertmannite particle in Figure 3b from the Tinto Santa Rosa mine. The inset in the left image shows a magnified area of the lattice fringes enclosed by the solid-line white box. The image on the right shows the tips of the same needles seen in the left image. The insets in the right image show the FFT patterns of the areas enclosed by the dashed-line white boxes. See text for details.

**TABLE 5.** The  $d$ -spacings measured from FFT analysis of lattice fringes (Fig. 6) and the corresponding peak in the schwertmannite and goethite XRD patterns\*

Image area	Schwertmannite XRD peak (nm)	Goethite planes
Inset left image		
0.503 nm $\pm$ 0.010	0.486	(200)
A,B,C,D	0.255	A–D: (301), (210); B–D: (011); D: (400)
A,C,D	0.339	No known plane [H <sub>2</sub> O-jarosite†: (113) (015) (202)]
A,B,C	0.228	(401)

\* See Supplemental Figure 5' for exact locations of  $d$ -spacings, including error bars.  
† Majzlan et al. (2004b).

**TABLE 6.** The  $d$ -spacings measured from FFT analysis of lattice fringes (Fig. 7) and the corresponding peak in the schwertmannite goethite, and H<sub>2</sub>O-jarosite XRD patterns\*

Image area	Schwertmannite XRD peak (nm)	Goethite planes
A,B	0.255	A: (301) (210); A,B: (111) (400) (011)
A,B,C,D,E	0.228	A–E: (401) (202); A–C: (211); C: (002)
A	0.195	(202) (311)
X: 0.238 nm $\pm$ 0.006	0.255/0.228	(111)

\* See Supplemental Figure 6' for exact location of  $d$ -spacings, including error bars.

modeling (Table 2) did not predict that these sites were supersaturated with respect to H<sub>2</sub>O-jarosite, hence this phase is not shown in Tables 5 and 6, but H<sub>2</sub>O-jarosite has been observed in other field studies on the TSR site (Asta et al. 2010b). One set of lattice fringes visible near the base of the needle (Fig. 6 inset, left image; Table 5) has a  $d$ -spacing that closely aligns with the 0.486 nm peak of schwertmannite. Goethite's (200) plane has a reflection in the range of this  $d$ -spacing. Few areas in any of the needles that we imaged exhibit distinct outlines of individual nanoparticles, but inset area X in Figure 7 shows lattice fringes that form the edges of a 5 nm particle within the needle.

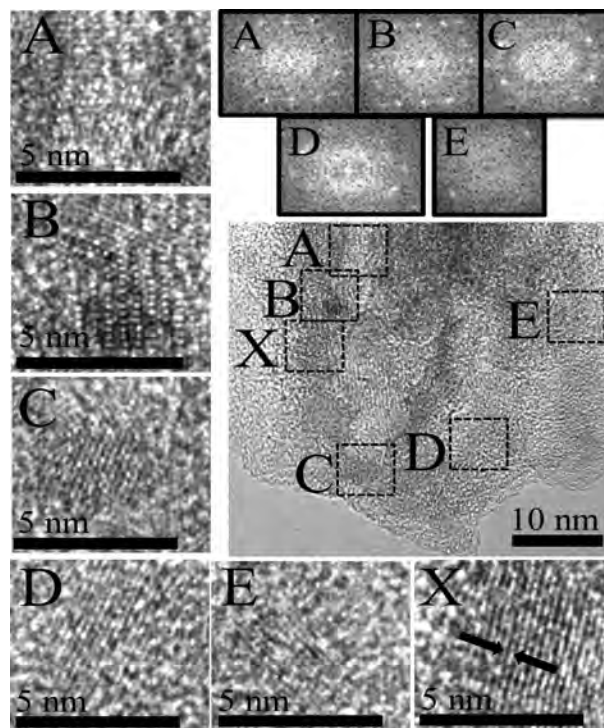


**FIGURE 7.** HRTEM images of needles on the surface of a schwertmannite particle from the Tinto Santa Rosa mine. Insets A–E show the FFT patterns of areas enclosed by their corresponding dashed-line black boxes. The inset "X" shows lattice fringes from area "X" enclosed by a dashed-line black box. See text for details.

At the scale of the bulk sample the schwertmannite from the MR and TSR mine sites appear similar. Their XRD patterns are nearly identical with matching peak positions and the digestion of the bulk material shows that the iron and sulfur content differs at most by approximately 1 wt%. However, the HRTEM

reveals differences between these samples that are not possible to see using bulk analysis. The images in this study show that the TSR schwertmannite samples contain schwertmannite particles with needles that are crystalline with easily visible lattice fringes and with FFT analyses displaying multiple bright spots. Though outlines of individual crystals within the needles are not discernable, the blotchy contrast displayed in multiple TSR schwertmannite aggregates in this study (Figs. 3b and 6; Supplemental Figs. 7<sup>1</sup> and 8<sup>1</sup>) indicates rounded particles aggregated together. This stands in contrast to the more uniform contrast of the MR schwertmannite needles (Figs. 4 and 5, and Supplemental Fig. 8<sup>1</sup>) where lattice fringes are rarely visible and FFT patterns exhibit few or no bright spots at all. Unfortunately, due to the practical limits of TEM, it is not possible to determine if all schwertmannite particles in both samples would exhibit the same trends as those described above. However, all figures in this study represent the data collected on multiple needles of three different aggregates of schwertmannite from these samples.

Regardless of the differences between these two schwertmannite samples they may, eventually, transform to goethite or jarosite. Previous field studies on both the MR and TSR sites reported an evolution of schwertmannite to goethite and jarosite in samples taken from the surface precipitates down to the deeper and older sediments (Acero et al. 2006; Asta et al. 2010a). Acero et al. (2006) also observed this transformation from natural schwertmannite to goethite and jarosite in the laboratory, but other studies reported the transformation of synthetic schwertmannite solely to goethite (Bigham et al. 1996b; Burton et al. 2008; Jonsson et al. 2005; Knorr and Blodau 2007; Regenspurg et al. 2004; Schwertmann and Carlson 2005). The proposed transformation mechanism is the dissolution of schwertmannite accompanied by simultaneous precipitation of goethite, as evidenced by the release of sulfate and the uptake of hydroxyls from solution (Bigham et al. 1996b).

In this study, the agreement between the *d*-spacings measured from individual lattice fringes and the *d*-spacings for goethite and H<sub>3</sub>O-jarosite planes suggests that transformation from schwertmannite to goethite may occur via atomic rearrangement with aging within the schwertmannite needles themselves. The kinetics of the schwertmannite to goethite transformation are not well understood and the transformation times can range from hours (Burton et al. 2008) to months (Knorr and Blodau 2007; Regenspurg et al. 2004; Schwertmann and Carlson 2005) to years (Bigham et al. 1996b; Jonsson et al. 2005; Regenspurg et al. 2004). It is also important to note again that the differences observed in crystallinity using HRTEM are not visible in the XRD pattern and therefore previous kinetics studies that relied solely on XRD would not observe the initial aging steps that are suggested in this study.

Similar aging phenomena have been observed in the conversion of ferrihydrite to goethite (Banfield et al. 2000) and in the weathering of silicate minerals (Hochella and Banfield 1995), where structural inheritance during phase transformation occurs. In their proposed model structure for schwertmannite, Fernandez-Martinez et al. (2010) noted the close relationship between the iron octahedral framework of schwertmannite and goethite. The authors of that paper pointed out that the release of just one pair of iron octahedra would allow the transformation from a

schwertmannite to a goethite framework. A strong relationship between the structures of goethite and schwertmannite is also apparent in the schwertmannite XRD pattern. The most intense peak of the schwertmannite XRD pattern at 0.255 nm—where the majority of lattice fringes were observed—overlaps with the second (111) and third (301) most intense reflections in the goethite XRD pattern (Cornell and Schwertmann 2003). Based on this it is conceivable that the small amount of observable order in the schwertmannite XRD pattern could be due to goethite nanoparticles within the schwertmannite matrix. A previous study on synthetic schwertmannite produced at 85 °C showed that schwertmannite nanoneedles were entirely composed of faceted goethite nanocrystals (Hockridge et al. 2009). Although there is no observable evidence of distinctive faceted goethite nanocrystals in the natural schwertmannite nanoneedles in this study, the Hockridge et al. (2009) study demonstrates that the goethite structure may have some similarity to the schwertmannite structure. This was observed despite the fact that individual goethite peaks in the XRD pattern cannot be identified.

Although proving this model is beyond the scope of this study, it is worth noting that schwertmannite's initial stability as a nanomineral, but its eventual transformation to a bulk phase of goethite, may be explained by the Ostwald step rule as explained by Navrotsky (2004). Navrotsky points out that with increasing metastability and increasing surface area, surface energy decreases. For this reason certain polymorphs (e.g., anatase, one of the polymorphs of titania) and amorphous phases (e.g., amorphous zirconia) are favored at smaller crystal sizes. It also follows that metastable phases will be formed initially rather than bulk phases during crystal growth as a lower surface energy results in a lower maximum free energy barrier and smaller size for the "critical radius" of a nucleating particle. The "critical radius" is the size at which particles will spontaneously grow larger. However, although Navrotsky does not point to a particular example, she acknowledges that the Ostwald step rule, even as modified by her, does not take into account kinetic factors. The Ostwald step rule assumes that the kinetics will follow the same path as laid out by thermodynamics. This model works well for ceramics where temperatures are high. However, in low-temperature systems, rate-limiting steps may be the defining characteristic for crystal growth.

These rate-limiting steps may be important if schwertmannite forms from many possible species in solution including ions, small molecules, clusters, and nanoparticles. For example, Majzlan and Myneni (2005) found that Fe<sup>III</sup> oligomers that are hydrogen-bonded to sulfate are present in acid sulfate waters typical of AMD. The rate of attachment and detachment of these species to a growing heterogeneous crystal surface is not well understood and these processes may occur at different times on different areas of the growing crystal. Schwertmannite's highly disordered and polyphasic character suggests that this may be the case for this mineral. Therefore, although thermodynamics may explain why a nanomineral would be formed at all over merely precipitating a bulk phase, kinetics may play the predominant role in governing schwertmannite's morphology, structure, and in situ transformation. Future studies on schwertmannite could begin to address this possibility as a way to explain the heterogeneous structure observed in this study.

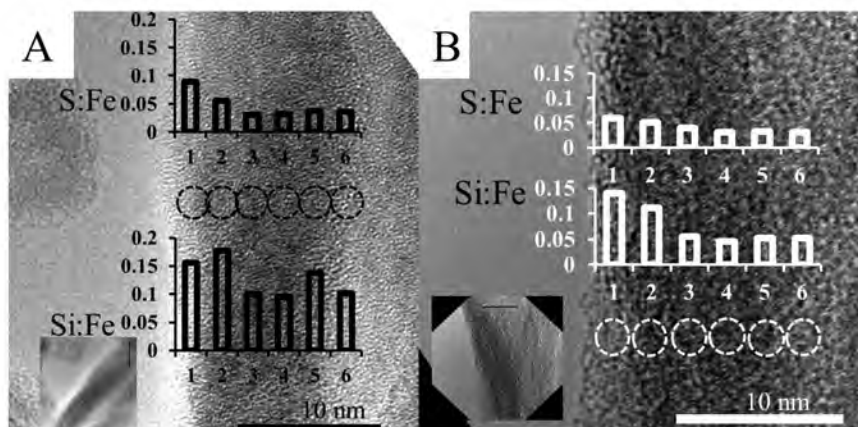


**FIGURE 8.** HRTEM images of needles on the surface of a schwertmannite particle from the Monte Romero mine. Insets show the larger area where the images were taken. The black (a) and white (b) circles show the areas where EDX data was collected. Bar graphs show the ratio of integrated K-peak intensities from EDX spectra for sulfur to iron (S:Fe) and silicon to iron (Si:Fe). See text for details.

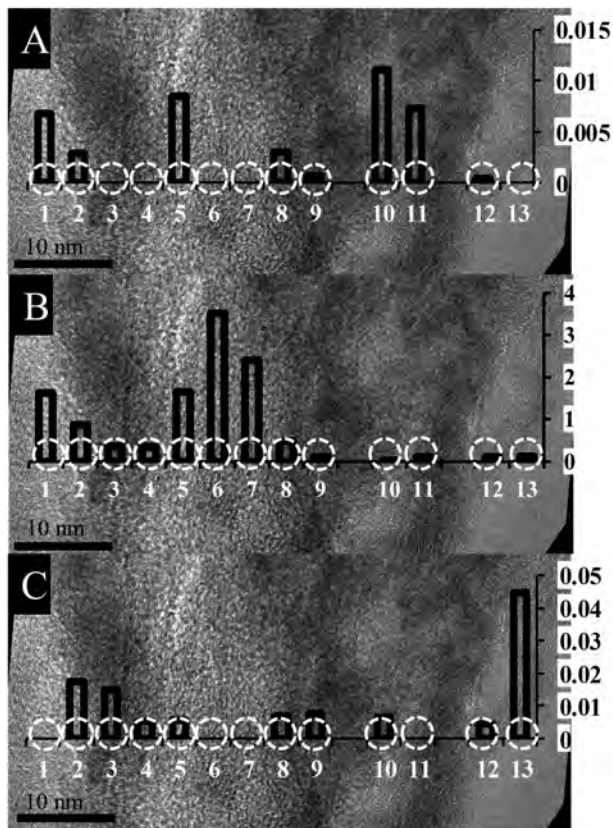


**FIGURE 9.** Schwertmannite nanoneedles from the Tinto Santa Rosa sample (for larger view see Supplemental Fig. 1<sup>1</sup>), with the needle surface on the far right side of the image. The white circles show the location where the EDX data was collected. Bar graphs show the ratio of integrated K-peak intensities from EDX spectra for sulfur to iron (S:Fe) (a), silicon to iron (Si:Fe) (b), and arsenic to iron (As:Fe) (c). The ratios of sulfur to iron and silicon to iron may be directly compared to each other (see text), but the arsenic to iron ratios should not be directly compared to the ratios of the other elements. See text for details.

#### The presence of sulfur and silicon in schwertmannite nanoneedles

Assuming that the schwertmannite needles may have a cone-like shape, the EDX data implies a heterogeneous distribution of sulfur in the schwertmannite needles. The ratio of sulfur to iron is higher on the surface of the schwertmannite needles in the Monte Romero schwertmannite than in the center of the needle (Fig. 8). Surprisingly, considering that the concentration of sulfur is much greater than silicon in the bulk sample (Table 3), silicon has a higher concentration than sulfur in the individual needles. The silicon to iron ratio is also higher on the surface than in the center of the needles.

EDX analysis of the TSR schwertmannite shows that the concentration of sulfur is two orders of magnitude lower than silicon in the needles (Fig. 9). Again, this is a surprising result considering the bulk chemical information (Table 3) where sulfur is two orders of magnitude higher in concentration than silicon. In the needles, the highest concentration of sulfur occurs in close proximity to the darker contrast areas with easily observable lattice fringes. In contrast silicon occurs in the highest concentration in the areas between the needles (see sampling points 5–7, Figs. 9a and 9b). In other needles on the same schwertmannite particle, there is a high concentration of sulfur in areas with visible lattice fringes, further showing evidence of the close association of sulfur with the more crystalline and lower silicon to iron ratio areas (Supplemental Fig. 10<sup>1</sup>). This is reasonable as a sulfate molecule may fit in the proposed iron octahedral tunnel structure of schwertmannite and may also complex with the surface of the schwertmannite (Bigham et al. 1994; Fernandez-Martinez et al. 2010). Sulfate is not a part of the structure of goethite, however, but may sorb to the surface of iron oxides (McBride 1994). Sulfate being released to solution as the needles transform to goethite may also explain the higher ratio of sulfur to iron on the surface, compared to the core of the needles. Previous studies explained higher concentrations of sulfate in bulk digestions of samples than would be predicted by the proposed chemical formula for schwertmannite as sulfate that is adsorbed to the surface of schwertmannite (Bigham et al. 1996a).

Silicon, unlike sulfate, has never been suggested to play any role in previously proposed schwertmannite structures. Under the geochemical conditions of the MR and TSR field sites the majority of silicon should be in the monosilicic acid form ( $\text{H}_4\text{SiO}_4$ ). As the water samples were undersaturated with respect to amorphous silica and these samples were collected in waters with a pH of 3, which is much less than the  $\text{pK}_1$  of silicic acid (McBride 1994), silica most likely adsorbed to the surface of the schwertmannite. Although surface adsorbed silica has not been observed for schwertmannite in any previous studies, silicic acid may form complexes and polymers at the surface of iron (oxyhydr)oxide surfaces (Doelsch et al. 2001, 2003; Eick et al. 2009; Waltham and Eick 2002). Surface adsorption may also increase within the nano- and mesopores created by the closely packed needles of schwertmannite because they create highly confined spaces where water activity will be reduced as compared to bulk water. This reduces the hydration of species and therefore promotes inner-sphere complexation (Wang et al. 2003).

Silicon was measurable in multiple needles from this same TSR schwertmannite aggregate as well as in another aggregate of TSR schwertmannite that were randomly selected (Supplemental Figs. 11 and 12<sup>1</sup>). The pattern of high silicon to iron ratios in amorphous areas was also observed repeatedly (Supplemental Fig. 11<sup>1</sup>). Although it was not possible to collect chemical information on the amount of silicon present in the interior of schwertmannite in these studies, the ratio of silicon to iron from the bulk digestion and from EDX data on entire aggregates of schwertmannite indicates that this high ratio of silicon to iron is a surface phenomenon. It is also possible that only those particles that had higher than average concentrations of silicon on the surface were observed in this study. Determining what effect silicon could have on the structure of schwertmannite is beyond the scope of the current study. Recently though, a study on natural ferrihydrite that contained 2–9 wt% silica proposed that silica reduced particle size and increased structural disorder in the ferrihydrite particles (Cismasu et al. 2011). Other studies also found that silica inhibits iron polymerization and complexes with the surface of iron oxides (Pokrovski et al. 2003). Regardless of the exact role of silicon associated with schwertmannite, its presence in our samples adds to the already complex nature of understanding the surface reactivity of naturally occurring nanominerals.

### The distribution of arsenic within schwertmannite needles

According to the bulk digestion of the two schwertmannite samples, the TSR sample contains approximately twice the concentration of arsenic as the MR sample. While arsenic was detectable via TEM/EDX in needles in the TSR sample (Fig. 9c), arsenic was not detected in the MR sample. The EDX results indicate that arsenic in the TSR sample was strongly associated with the darker contrast and more highly crystalline areas of the schwertmannite surface (Fig. 9c, sampling points 2–5 and 8–10; Supplemental Fig. 13<sup>1</sup>) with the exception of point 13 where there is a lighter contrast. However, the point 13 area also contains lattice fringes and has relatively low silicon to iron ratio indicating that the difference in contrast is likely due to differences in thickness or local diffraction conditions and not crystallinity. The absence of arsenic in areas high in silicon is also consistent with previous work where silicate reduced the rate of

adsorption, blocked adsorption sites, and displaced arsenite on goethite surfaces (Luxton et al. 2008; Waltham and Eick 2002).

Field studies (Acero et al. 2006; Asta et al. 2010b) explained the sequestration of arsenic by schwertmannite through the exchange of the sulfate anion by the arsenate anion in the tunnels of the akaganéite-like proposed structure for schwertmannite or through surface adsorption (Fukushi et al. 2004; Regenspurg and Peiffer 2005; Waychunas et al. 1994). Geochemical modeling predicts that the dominant arsenic species will be the arsenate anion ( $\text{H}_2\text{AsO}_4^-$ ) (Dove and Rimstidt 1985) in the field sites where our samples were collected (Acero et al. 2006; Asta et al. 2010b). Schwertmannite has a point of zero charge of 7.2 (Jonsen et al. 2005) favoring sorption of negatively charged ions at a low pH where the surface of schwertmannite has a positive charge (Acero et al. 2006). While arsenic may be sequestered by schwertmannite, it can also inhibit its formation and transformation to goethite (Regenspurg and Peiffer 2005; Waychunas et al. 1994). Both sulfate and arsenate inhibit the formation of the ferric hydroxyl complex [ $\text{Fe(III)-OH}^-$ ] and therefore iron oxide formation (Majzlan and Myneni 2005; Regenspurg and Peiffer 2005). Arsenate acts as a more “aggressive” competitor anion than sulfate as the stability constant for Fe(III) and arsenate ( $\log K = 29.3$ ) is much higher than the stability constant for Fe(III) and sulfate ( $\log K = 7.78$ ) (Carlson et al. 2002; Dzombak and Morel 1990; Regenspurg and Peiffer 2005). In the study presented here though, the higher concentration of arsenic was observed in the more crystalline TSR sample (Fig. 9c) with observable lattice fringes whose spacings closely matched those of goethite (Supplemental Figs. 5 and 6<sup>1</sup>). The natural schwertmannite from the TSR site contained 10 times less arsenic than the synthetic schwertmannite used in Regenspurg et al.’s (2005) study and therefore it is likely that arsenic does not have a highly inhibitory effect on goethite formation at these trace levels. Studies on the formation of iron oxides in the presence of silicon also found that silicon inhibits the formation of crystalline iron oxides and instead favors the precipitation of hydrous ferric oxide and ferrihydrite (Voegelin et al. 2010).

The presence of arsenic associated with goethite nanocrystals possibly forming within the highly disordered schwertmannite needle matrix has interesting implications for the fate of this trace element once the transformation to goethite has occurred. In laboratory studies, the solid phase retained arsenic throughout the transformation from schwertmannite to goethite, but no specific mechanisms were proposed for this retention (Acero et al. 2006; Courtin-Nomade et al. 2005). Although the ionic radius for arsenate would, theoretically, allow it to be incorporated into the goethite structure (Cornell and Schwertmann 2003), this has not been demonstrated prior to the study by Pedersen et al. (2006). This study found that arsenate could be very strongly bound to goethite and incorporated into the structure, preventing it from desorbing. Previous studies also demonstrated the high affinity of goethite nanocrystals for arsenic in river systems (Plathe et al. 2010), allowing goethite nanocrystals to act as a transporter for trace elements over long distances or “nanovectors” (Hasselov and von der Kammer 2008). The combined effect of a strong affinity for goethite and the inhibition of crystal growth by arsenic increases the likelihood that schwertmannite derived goethite would be a source of these nanovectors for arsenic transport. Fur-

thermore, regardless of the presence of arsenic, goethite formed from the transformation of schwertmannite forms nanocrystals (Bigham et al. 1996b; French et al., in preparation). A survey on the Iberian Pyrite Belt (IPB) concluded that the majority of goethite in that system should be considered as a transformation product of schwertmannite, as goethite was most often associated with older precipitates and schwertmannite with the overlying fresh precipitates (España et al. 2005). Olías et al. (2006) found that over 36 tons per year of “dissolved” arsenic in the Odiel and Tinto rivers (that is, arsenic that passes through a 0.45  $\mu\text{m}$  filter, and therefore allowing particles <450 nm to pass through) are released to the Huelva estuary and then to the Atlantic ocean. Although determining whether or not there is a significant nanoparticulate load in the Odiel and Tinto rivers requires further research, clearly the strong relationship between schwertmannite, goethite, and arsenic in the IPB makes schwertmannite one of the major geochemical controls on the global arsenic flux.

### Schwertmannite as a “mineral”

Currently, minerals are most commonly defined as naturally occurring substances, produced by (bio)geochemical processes, with a highly ordered, repeating atomic arrangement (a crystalline substance) whose composition can be described by a chemical formula that is either fixed or variable (or, also as often stated, a definite, but not necessarily fixed, composition). Samples of the same mineral vary in terms of minor and/or trace element composition, and in the case of solid solution, major element composition as long as these substitutions do not change the crystal structure. Finally, it follows that minerals of the same major and minor element composition will express a set of measureable and consistent physical and chemical properties.

However, as science and technology progress, and mineralogical subjects continue to develop, many have considered broadening the definition of how minerals are presently defined e.g., Klein and Dutrow (2008). One area of expansion concerns what are now known as nanominerals and mineral nanoparticles (Hochella 2008). Most nanominerals and mineral nanoparticles satisfy the definition of a mineral as described above, except for one major difference: as they get smaller, it becomes likely that their physical properties will change, sometimes dramatically, as a function of their size and shape.

In this paper, we have considered schwertmannite to be a nanomineral because its rod- or needle-like morphology is always in the nanometer size range. These nanoneedles are never observed to grow to macroscopic sizes either in the lab or in the field. However, as presented in this paper, there are additional complicating factors. For example, the variable atomic structure observed in schwertmannite nanoneedles includes ordered regions that are only coherent over a few to several nanometers, as well as regions that show little to no atomic order between and among the ordered regions. Many ordered regions display diagnostic *d*-spacings of goethite or jarosite, schwertmannite’s principal transformation products. Some of these *d*-spacings are also in the range that generate peaks characteristic of the schwertmannite XRD pattern. From such small ordered regions, these would result in very broad X-ray diffraction lines, as observed. Compositionally, although the measured amounts of iron and sulfur are consistent between bulk samples in this study, and also

agree well with previous studies of schwertmannite, the measured sulfur to iron ratios at nanometer spatial resolution near the edges of needles vary considerably. Also, although silicon is a minor component, its concentration can be much higher at least near the surface of needles. Considering this, there is little wonder why the measured solubility product of schwertmannite is so variable, to the point of being only marginally useful.

Taken together for schwertmannite, nearly every aspect of the definition of a mineral has been called into question. Therefore, in a strict sense, one might conclude that schwertmannite is not a mineral, nor is it a true mineraloid (a mineral-like substance that is not crystalline, a common example being the volcanic glass obsidian). It is well beyond the scope of this paper to try to resolve this issue. Allowing the definition of a mineral to become more inclusive, rather than exclusive, is surely a debatable matter. However this is resolved, the most important point to be made here is that schwertmannite plays a central role in natural systems and we must develop a rational mineralogical and geochemical framework to deal with it.

### ACKNOWLEDGMENTS

We thank the ICTAS Nanoscale Characterization and Fabrication Laboratory (NCFL) at Virginia Tech, the Materials Science and Engineering Nanoscale Materials Characterization Facility (MSE-NMCF) at the University of Virginia, and the Campus Electron Optics Facility (CEOF) at Ohio State University in collaboration with FEI Company (Jan Ringnalda and John Caola) for the use of their Titan microscopes. We thank Matthew Eick for helpful comments that greatly enhanced the quality of this paper. Grants from the U.S. Department of Energy (DE-FG02-06ER15786) and the Institute for Critical Technology and Applied Sciences at Virginia Tech provided major financial support for this project. We are also appreciative of the support from the National Science Foundation (NSF) and the Environmental Protection Agency through the Center for Environmental Implications of NanoTechnology (CEINT) funded under NSF Cooperative Agreement EF-0830093. Fellowship support for this research was provided by the National Science Foundation (NSF IGERT grant DGE-0504196). Any opinions, findings, and conclusions or recommendations expressed in this material are those of the authors and do not necessarily reflect the views of NSF, EPA, or DOE.

### REFERENCES CITED

- Abramoff, M.D., Magalhaes, P.J., and Ram, S.J. (2004) Image processing with ImageJ. *Biophotonics International*, 11, 36–42.
- Acero, P., Ayora, C., Torrento, C., and Nieto, J.M. (2006) The behavior of trace elements during schwertmannite precipitation and subsequent transformation into goethite and jarosite. *Geochimica et Cosmochimica Acta*, 70, 4130–4139.
- Asta, M.P., Ayora, C., Acero, P., and Cama, J. (2010a) Field rates for natural attenuation of arsenic in Tinto Santa Rosa acid mine drainage (SW Spain). *Journal of Hazardous Materials*, 177, 1102–1111.
- Asta, M.P., Ayora, C., Roman-Ross, G., Cama, J., Acero, P., Gault, A.G., Charnock, J.M., and Bardelli, F. (2010b) Natural attenuation of arsenic in the Tinto Santa Rosa acid stream (Iberian Pyritic Belt, SW Spain): The role of iron precipitates. *Chemical Geology*, 271, 1–12.
- Ball, J.W. and Nordstrom, D.K. (1991) User’s manual for WATEQ4F with revised thermodynamic database and test cases for calculating speciation of major, trace, and redox elements in natural waters. U.S. Geological Survey. *Water-Resources*.
- Banfield, J.F., Welch, S.A., Zhang, H.Z., Ebert, T.T., and Penn, R.L. (2000) Aggregation-based crystal growth and microstructure development in natural iron oxyhydroxide biomineralization products. *Science*, 289(5480), 751–754.
- Bigham, J.M. and Nordstrom, D.K. (2000) Iron and aluminum hydroxysulfates from acid sulfate waters. In C.N. Alpers, J.L. Jambor, and D.K. Nordstrom, Eds., *Sulfate Minerals—Crystallography, Geochemistry and Environmental Significance*, 40, p. 351–403. Reviews in Mineralogy and Geochemistry, Mineralogical Society of America, Chantilly, Virginia.
- Bigham, J.M., Carlson, L., and Murad, E. (1994) Schwertmannite, a new iron oxyhydroxysulphate from Pyhasalmi, Finland, and other localities. *Mineralogical Magazine*, 58(393), 641–648.
- Bigham, J.M., Schwertmann, U., and Pfab, G. (1996a) Influence of pH on mineral speciation in a bioreactor simulating acid mine drainage. *Applied Geochemistry*, 11, 845–849.
- Bigham, J.M., Schwertmann, U., Traina, S.J., Winland, R.L., and Wolf, M. (1996b) Schwertmannite and the chemical modeling of iron in acid sulfate waters.

- Geochimica et Cosmochimica Acta, 60, 2111–2121.
- Blodau, C. (2006) A review of acidity generation and consumption in acidic coal mine lakes and their watersheds. *Science of the Total Environment*, 369, 307–332.
- Burton, E.D., Bush, R.T., and Sullivan, L.A. (2006) Sedimentary iron geochemistry in acidic waterways associated with coastal lowland acid sulfate soils. *Geochimica et Cosmochimica Acta*, 70, 5455–5468.
- Burton, E.D., Bush, R.T., Sullivan, L.A., and Mitchell, D.R.G. (2007) Reductive transformation of iron and sulfur in schwertmannite-rich accumulations associated with acidified coastal lowlands. *Geochimica et Cosmochimica Acta*, 71, 4456–4473.
- Burton, E.D., Bush, R.T., Sullivan, L.A., and Mitchell, D.R.G. (2008) Schwertmannite transformation to goethite via the Fe(II) pathway: Reaction rates and implications for iron-sulfide formation. *Geochimica et Cosmochimica Acta*, 72, 4551–4564.
- Caraballo, M.A., Rötting, T.S., Nieto, J.M., and Ayora, C. (2009) Sequential extraction and DDXRD applicability to poorly crystalline Fe- and Al-phase characterization from an acid mine water passive remediation system. *American Mineralogist*, 94, 1029–1038.
- Caraballo, M.A., Sarmiento, A.M., Sanchez-Rodas, D., Nieto, J.M., and Parvainen, A. (2011) Seasonal variations in the formation of Al and Si rich Fe-stromatolites, in the highly polluted acid mine drainage of Agua Agria Creek (Tharsis, SW Spain). *Chemical Geology*, 284, 97–104.
- Carlson, L., Bigham, J.M., Schwertmann, U., Kyek, A., and Wagner, F. (2002) Scavenging of As from acid mine drainage by schwertmannite and ferrihydrite: A comparison with synthetic analogues. *Environmental Science & Technology*, 36, 1712–1719.
- Cismasu, A.C., Michel, F.M., Tcaciuc, A.P., Tyliczszak, T., and Brown, G.E. (2011) Composition and structural aspects of naturally occurring ferrihydrite. *Comptes Rendus Geoscience*, 343, 210–218.
- Cornell, R.M. and Schwertmann, U. (2003) *The Iron Oxides*. Wiley-VCH, Weinheim.
- Courtin-Nomade, A., Grosbois, C., Bril, H., and Roussel, C. (2005) Spatial variability of arsenic in some iron-rich deposits generated by acid mine drainage. *Applied Geochemistry*, 20, 383–396.
- Doelsch, E., Stone, W.E.E., Petit, S., Mason, A., Rose, J., Bottero, J.Y., and Nahon, D. (2001) Speciation and crystal chemistry of Fe(III) chloride hydrolyzed in the presence of SiO<sub>4</sub> ligands. 2. Characterization of Si-Fe aggregates by FTIR and Si-29 solid-state NMR. *Langmuir*, 17, 1399–1405.
- Doelsch, E., Mason, A., Rose, J., Stone, W.E.E., Bottero, J.Y., and Bertsch, P.M. (2003) Chemistry and structure of colloids obtained by hydrolysis of Fe(III) in the presence of SiO<sub>4</sub> ligands. *Colloids and Surfaces A-Physicochemical and Engineering Aspects*, 217, 121–128.
- Dove, P.M. and Rimstidt, J.D. (1985) The solubility and stability of scorodite, FeAsO<sub>4</sub>·2H<sub>2</sub>O. *American Mineralogist*, 70, 838–844.
- Dzombak, D.A. and Morel, F.M.M. (1990) *Surface Complexation Modeling—Hydrous Ferric Oxide*. Wiley-Interscience, New York.
- Eick, M.J., Luxton, T.P., and Welsh, H.A. (2009) Effect of silica polymerization on the oxalate-promoted dissolution of goethite. *Clays and Clay Minerals*, 57, 578–585.
- Espana, J.S., Pamo, E.L., Santofimia, E., Aduvire, O., Reyes, J., and Baretino, D. (2005) Acid mine drainage in the Iberian Pyrite Belt (Odiel river watershed, Huelva, SW Spain): Geochemistry, mineralogy and environmental implications. *Applied Geochemistry*, 20, 1320–1356.
- Fernandez-Martinez, A., Timon, V., Roman-Ross, G., Cuervo, G.J., Daniels, J.E., and Ayora, C. (2010) The structure of schwertmannite, a nanocrystalline iron oxyhydroxysulfate. *American Mineralogist*, 95, 1312–1322.
- Fernandez-Remolar, D., Gomez-Elvira, J., Gomez, F., Sebastian, E., Martini, J., Manfredi, J.A., Torres, J., Kesler, C.G., and Amils, R. (2004) The Tinto River, an extreme acidic environment under control of iron, as an analog of the Terra Meridiana hematite site of Mars. *Planetary and Space Science*, 52, 239–248.
- Fukushi, K., Sato, T., Yanase, N., Minato, J., and Yamada, H. (2004) Arsenate sorption on schwertmannite. *American Mineralogist*, 89, 1728–1734.
- Hasselov, M. and von der Kammer, F. (2008) Iron oxides as geochemical nanovectors for metal transport in soil-river systems. *Elements*, 4, 401–406.
- Hochella, M.F. (2008) Nanogeoscience: From origins to cutting-edge applications. *Elements*, 4, p. 373–380.
- Hochella, M.F. and Banfield, J.F. (1995) Chemical weathering of silicates in nature: a microscopic perspective with theoretical considerations. In A.F. White and S.L. Brantley, Eds., *Chemical Weathering Rates of Silicate Minerals*, 31, p. 353–406. Reviews in Mineralogy, Mineralogical Society of America, Chantilly, Virginia.
- Hochella, M.F., Moore, J.N., Golla, U., and Putnis, A. (1999) A TEM study of samples from acid mine drainage systems: Metal-mineral association with implications for transport. *Geochimica et Cosmochimica Acta*, 63, 3395–3406.
- Hockridge, J.G., Jones, F., Loan, M., and Richmond, W.R. (2009) An electron microscopy study of the crystal growth of schwertmannite needles through oriented aggregation of goethite nanocrystals. *Journal of Crystal Growth*, 311, 3876–3882.
- Janney, D.E., Cowley, J.M., and Buseck, P.R. (2000) Structure of synthetic 2-line ferrihydrite by electron nanodiffraction. *American Mineralogist*, 85, 1180–1187.
- Jonsson, J., Persson, P., Sjöberg, S., and Lovgren, L. (2005) Schwertmannite precipitated from acid mine drainage: phase transformation, sulphate release and surface properties. *Applied Geochemistry*, 20, 179–191.
- Kawano, M. and Tomita, K. (2001) Geochemical modeling of bacterially induced mineralization of schwertmannite and jarosite in sulfuric acid spring water. *American Mineralogist*, 86, 1156–1165.
- Kim, B., Park, C.S., Murayama, M., and Hochella, M.F. (2010) Discovery and characterization of silver sulfide nanoparticles in final sewage sludge products. *Environmental Science & Technology*, 44, 7509–7514.
- Klein, C. and Dutrow, B. (2008) *Mineral Science*. Wiley, New York.
- Knorr, K.H. and Blodau, C. (2007) Controls on schwertmannite transformation rates and products. *Applied Geochemistry*, 22, 2006–2015.
- Liu, J., Aruguete, D.M., Jinschek, J.R., Rimstidt, J.D., and Hochella, M.F. (2008) The non-oxidative dissolution of galena nanocrystals: Insights into mineral dissolution rates as a function of grain size, shape, and aggregation state. *Geochimica et Cosmochimica Acta*, 72, 5984–5996.
- Liu, J., Aruguete, D.M., Murayama, M., and Hochella, M.F. (2009) Influence of size and aggregation on the reactivity of an environmentally and industrially relevant nanomaterial (PbS). *Environmental Science & Technology*, 43, 8178–8183.
- Loan, M., Cowley, J.M., Hart, R., and Parkinson, G.M. (2004) Evidence on the structure of synthetic schwertmannite. *American Mineralogist*, 89, 1735–1742.
- Luxton, T.P., Eick, M.J., and Rimstidt, J.D. (2008) The role of silicate in the adsorption/desorption of arsenite on goethite. *Chemical Geology*, 252, 125–135.
- Majzlan, J. and Myneni, S.C.B. (2005) Speciation of iron and sulfate in acid waters: Aqueous clusters to mineral precipitates. *Environmental Science & Technology*, 39, 188–194.
- Majzlan, J., Navrotsky, A., and Schwertmann, U. (2004a) Thermodynamics of iron oxides: Part III. Enthalpies of formation and stability of ferrihydrite [~Fe(OH)<sub>3</sub>], schwertmannite [~Fe(O)(OH)<sub>3/4</sub>(SO<sub>4</sub>)<sub>1/8</sub>], and ε-Fe<sub>2</sub>O<sub>3</sub>. *Geochimica et Cosmochimica Acta*, 68, 1049–1059.
- Majzlan, J., Stevens, R., Boerio-Goates, J., Woodfield, B.F., and Navrotsky, A. (2004b) Thermodynamic properties, low-temperature heat-capacity anomalies, and single-crystal X-ray refinement of hydronium jarosite, (H<sub>3</sub>O)Fe<sub>3</sub>(SO<sub>4</sub>)<sub>2</sub>(OH)<sub>6</sub>. *Physics and Chemistry of Minerals*, 31, 518–531.
- Manceau, A. (2009) Evaluation of the structural model for ferrihydrite derived from real-space modelling of high-energy X-ray diffraction data. *Clay Minerals*, 44, 19–34.
- (2010) PDF analysis of ferrihydrite and the violation of Pauling's Principia. *Clay Minerals*, 45, 225–228.
- (2011) Critical evaluation of the revised akdalite model for ferrihydrite. *American Mineralogist*, 96, 521–533.
- McBride, M.B. (1994) *Environmental Chemistry of Soils*. Oxford University Press, New York.
- Michel, F.M., Ehm, L., Antao, S.M., Lee, P.L., Chupas, P.J., Liu, G., Strongin, D.R., Schoonen, M.A.A., Phillips, B.L., and Parise, J.B. (2007) The structure of ferrihydrite, a nanocrystalline material. *Science*, 316(5832), 1726–1729.
- Michel, F.M., Barron, V., Torrent, J., Morales, M.P., Serna, C.J., Boily, J.F., Liu, Q.S., Ambrosini, A., Cismasu, A.C., and Brown, G.E. (2010) Ordered ferrimagnetic form of ferrihydrite reveals links among structure, composition, and magnetism. *Proceedings of the National Academy of Sciences of the United States of America*, 107, 2787–2792.
- Moreau, J.W., Webb, R.I., and Banfield, J.F. (2004) Ultrastructure, aggregation-state, and crystal growth of biogenic nanocrystalline sphaerulite and wurtzite. *American Mineralogist*, 89, 950–960.
- Navrotsky, A. (2004) Energetic clues to pathways to biomineralization: Precursors, clusters, and nanoparticles. *Proceedings of the National Academy of Sciences of the United States of America*, 101, 12096–12101.
- Olias, M., Canovas, C.R., Nieto, J.M., and Sarmiento, A.M. (2006) Evaluation of the dissolved contaminant load transported by the Tinto and Odiel rivers (South West Spain). *Applied Geochemistry*, 21, 1733–1749.
- Parkhurst, D.L. (1995) User's guide to PHREEQC: a computer program for speciation, reaction path, advective-transport, and inverse geochemical calculations. U.S. Geological Survey. Water Resources.
- Pedersen, H.D., Postma, D., and Jakobsen, R. (2006) Release of arsenic associated with the reduction and transformation of iron oxides. *Geochimica et Cosmochimica Acta*, 70, 4116–4129.
- Peine, A., Tritschler, A., Kusel, K., and Peiffer, S. (2000) Electron flow in an iron-rich acidic sediment—evidence for an acidity-driven iron cycle. *Limnology and Oceanography*, 45, 1077–1087.
- Perez-Lopez, R., Asta, M.P., Roman-Ross, G., Nieto, J.M., Ayora, C., and Tucoulou, R. (2011) Synchrotron-based X-ray study of iron oxide transformations in terraces from the Tinto-Odiel river system: Influence on arsenic mobility. *Chemical Geology*, 280, 336–343.
- Pinedo-Vara, I. (1963) *Piritas de Huelva. Su historia, minería y aprovechamiento*. Summa, Madrid, Spain.

- Plathe, K.L., von der Kammer, F., Hasselov, M., Moore, J., Murayama, M., Hofmann, T., and Hochella, M.F. (2010) Using FIFFF and aTEM to determine trace metal-nanoparticle associations in riverbed sediment. *Environmental Chemistry*, 7, 82–93.
- Pokrovski, G.S., Schott, J., Garges, F., and Hazemann, J.L. (2003) Iron (III)-silica interactions in aqueous solution: Insights from X-ray absorption fine structure spectroscopy. *Geochimica et Cosmochimica Acta*, 67, 3559–3573.
- Raiswell, R., Benning, L.G., Davidson, L., Tranter, M., and Tulaczyk, S. (2009) Schwertmannite in wet, acid, and oxic microenvironments beneath polar and polythermal glaciers. *Geology*, 37, 431–434.
- Raiswell, R. (2011) Iron transport from the open continents to the open ocean: The aging-rejuvenation cycle. *Elements*, 7, 101–106.
- Regenspurg, S., Brand, A., and Peiffer, S. (2004) Formation and stability of schwertmannite in acidic mining lakes. *Geochimica et Cosmochimica Acta*, 68, 1185–1197.
- Regenspurg, S. and Peiffer, S. (2005) Arsenate and chromate incorporation in schwertmannite. *Applied Geochemistry*, 20, 1226–1239.
- Saez, R., Pascual, E., Toscano, M., and Almodovar, G.R. (1999) The Iberian type of volcano-sedimentary massive sulphide deposits. *Mineralium Deposita*, 34, 549–570.
- Sarmiento, A.M., Oliveira, V., Gomez-Ariza, J.L., Nieto, J.M., and Sanchez-Rodas, D. (2007) Diel cycles of arsenic speciation due to photooxidation in acid mine drainage from the Iberian Pyrite Belt (Sw Spain). *Chemosphere*, 66, 677–683.
- Schwertmann, U. and Carlson, L. (2005) The pH-dependent transformation of schwertmannite to goethite at 25°C. *Clay Minerals*, 40, 63–66.
- Tyler, G., Carrasco, R., Nieto, J.M., Perez, R., Ruiz, M.J., and Sarmineto, A.M. (2004) Optimization of major and trace element determination on acid mine drainage samples by ultrasonic nebulizer-ICP-OES (USN-ICP-OES). *Pittcon Conference*, p. 9000/1000, Chicago.
- Voegelin, A., Kaegi, R., Frommer, J., Vantelon, D., and Hug, S.J. (2010) Effect of phosphate, silicate, and Ca on Fe(III)-precipitates formed in aerated Fe(II)- and As(III)-containing water studied by X-ray absorption spectroscopy. *Geochimica et Cosmochimica Acta*, 74, 164–186.
- Waltham, C.A. and Eick, M.J. (2002) Kinetics of arsenic adsorption on goethite in the presence of sorbed silicic acid. *Soil Science Society of America Journal*, 66, 818–825.
- Wang, Y., Bryan, C., Xu, H., and Gao, H. (2003) Nanogeochemistry: Geochemical reactions and mass transfers in nanopores. *Geology*, 31, 387–390.
- Waychunas, G.A., Xu, N., Fuller, C.C., Davis, J.A., and Bigham, J.M. (1994) XAS study of As<sub>2</sub>O<sub>5</sub> and Se<sub>2</sub>O<sub>5</sub> substituted schwertmannites. 8th International Conference on X-Ray Absorption Fine Structure (XAFS VIII), p. 481–483, Berlin, Germany.
- Wu, C.H., Reynolds, W.T. Jr., and Murayama, M. (2012) A software tool for automatic analysis of selected area diffraction patterns within Digital Micrograph™. *Ultramicroscopy*, 112, 10–14.
- Yu, J.Y., Heo, B., Choi, I.K., Cho, J.P., and Chang, H.W. (1999) Apparent solubilities of schwertmannite and ferrihydrite in natural stream waters polluted by mine drainage. *Geochimica et Cosmochimica Acta*, 63, 3407–3416.

MANUSCRIPT RECEIVED OCTOBER 23, 2011

MANUSCRIPT ACCEPTED MAY 14, 2012

MANUSCRIPT HANDLED BY LARS EHM